Supporting Information

Synthesis of monodisperse rod-shaped silica particles through biotemplating of surface-functionalized bacteria

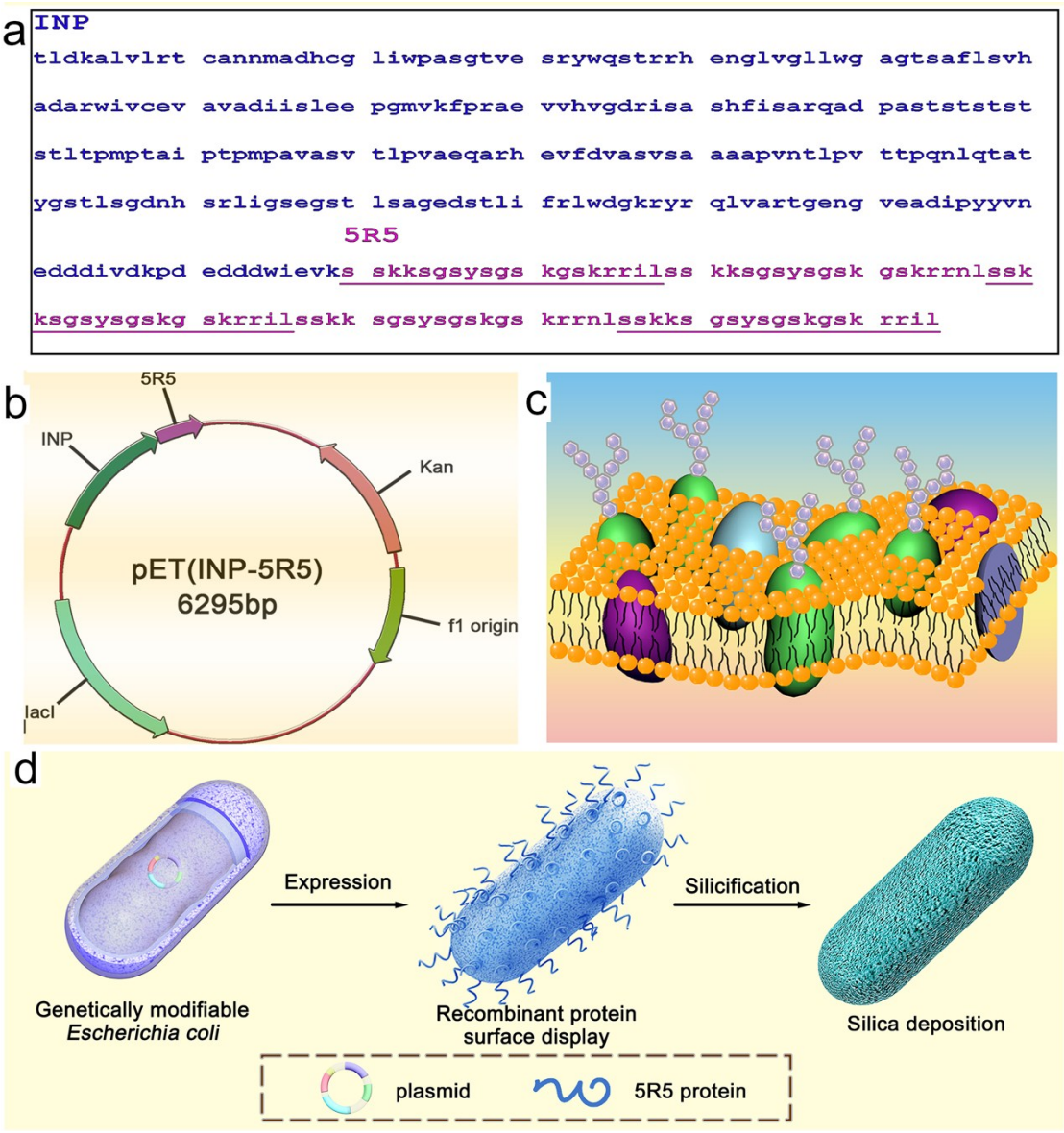

Figure S1. (a) The amino acid sequences of recombinant protein INP-5R5. 5R5 represents the five repeats of R5 sequence, in order to enhance the mineral-formation activity. (b) The map of plasmid pET(INP-5R5) encoding the recombinant protein INP-5R5. The protein 5R5 is genetically inserted to the downstream of INP, that serves as an anchor for 5R5 on the *E. coli* surface. (c) Schematic of cell surface display of 5R5. Carrier proteins anchor-INP (green ellipsoid) locate in the outer membrane, and target proteins-5R5 (gray sphere) are exposed to surrounding medium. INP is a stable carrier protein with high efficient, which can transport a fused protein through the complex cell envelope

structure and is resistant to attack or detachment[1]. (d) Schematic of surface display strategy for the silicification of *E. coli*.

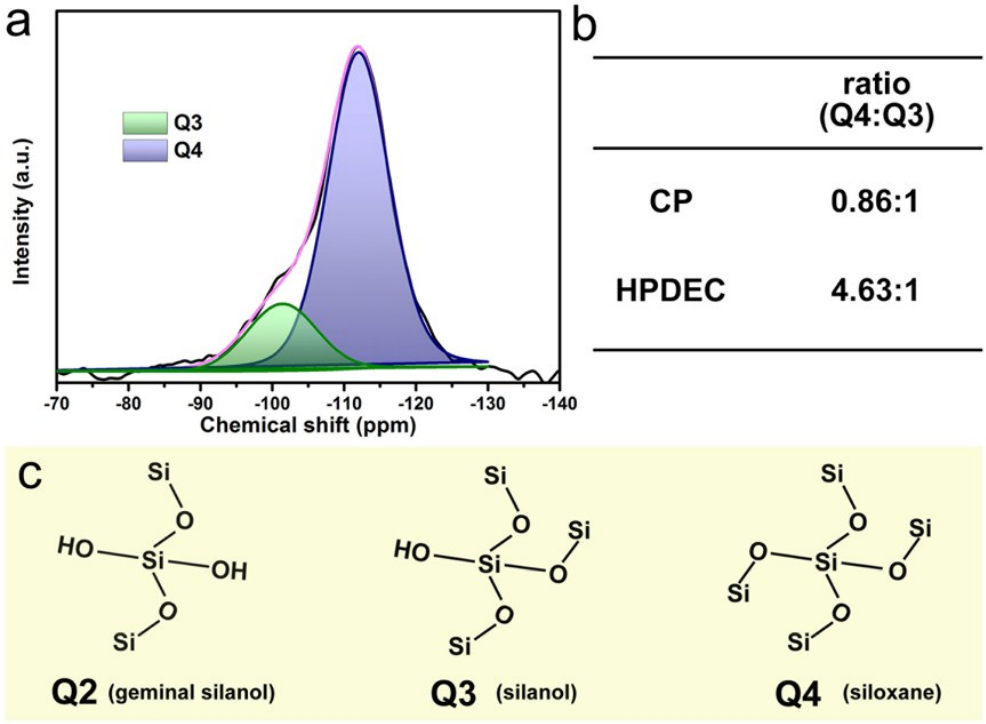

Figure S2. (a) ^{29}Si HPDEC NMR spectrum of 5R5-silica. (b) The ratio of Q4/Q3 in ^{29}Si CP and HPDEC spectra. (c) The chemical structures of Q2 (geminal silanol), Q3 (single silanol), and Q4 (bulk siloxane) in silica.

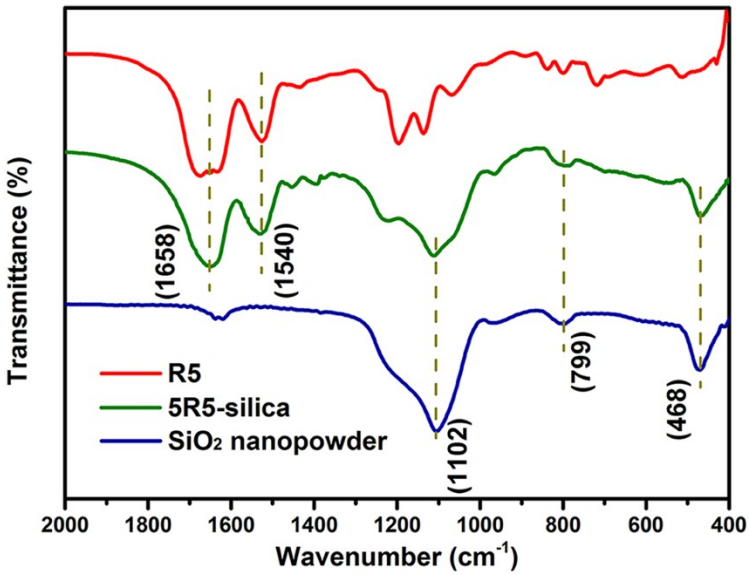

Figure S3. FITR spectra of R5, 5R5-silica and SiO_2 nanopowder.

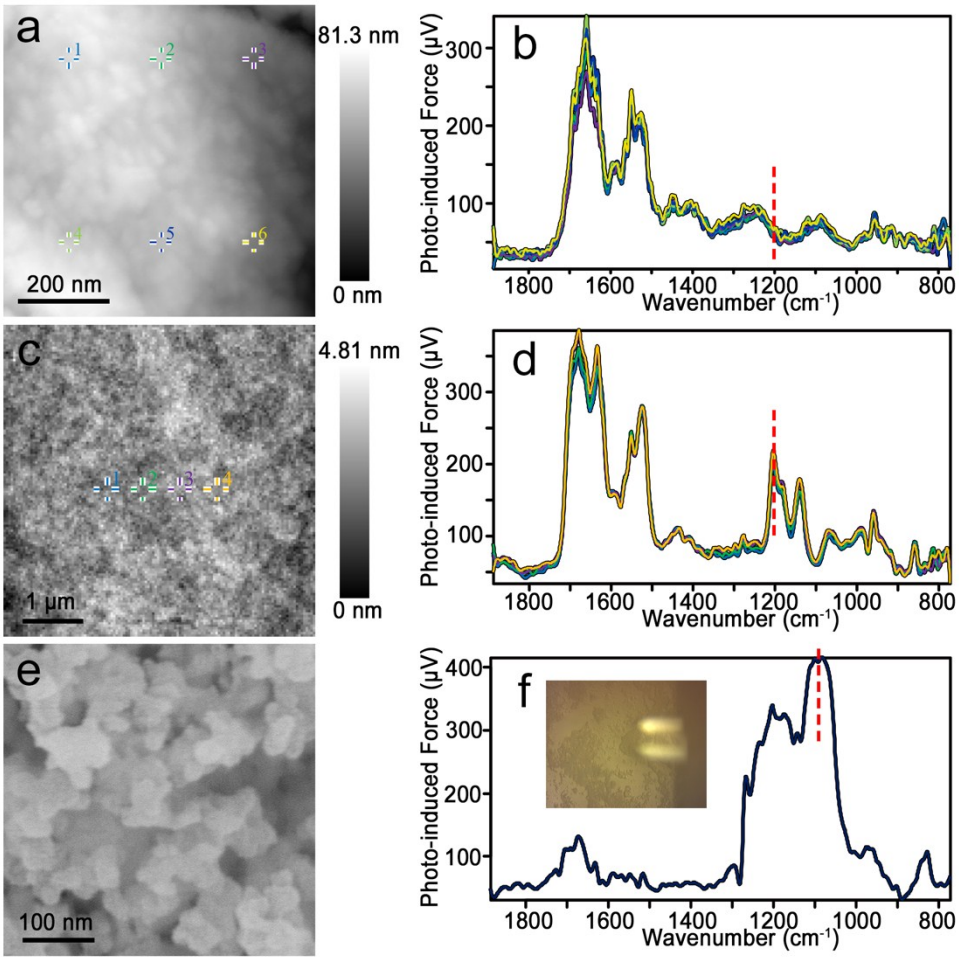

Figure S4. (a) Topography image of bare *E. coli*. The points of spectral acquisition are highlighted. (b) The PiFM spectra are across the bacterium's surface from (a). (c) Topography image of R5 peptide powder. The points of spectral acquisition are highlighted. (d) The PiFM spectra from the points in (c). (e) SEM image of commercial silica powder with the diameter of 8-10 nm. (f) The PiFM spectrum of silica powder.

E. coli shows two prominent peaks around 1650 and 1543 cm^{-1}, most likely amide peaks due to lipopolysaccharides on the surface of the bacterial cell wall. These peaks are also seen in R5. However, there are peaks at 1200 and 1120 cm^{-1} found in the protein spectra that are not in the *E. coli* spectra. These are the only peaks that can be used to identify the artificial protein from the surface of the *E. coli*. The silica spectrum shows a broad peak from 1020 to 1280 cm^{-1}, with a maximum around 1100 cm^{-1}. The peak around 1200 cm^{-1} would not usually be associated with silica (Figure S3), there is a possibility that the sample may be contaminated. PiFM imaging was carried out using 1100 cm^{-1} to highlight the silica and 1200 cm^{-1} to try to highlight the 5R5 protein instead the *E. coli*.

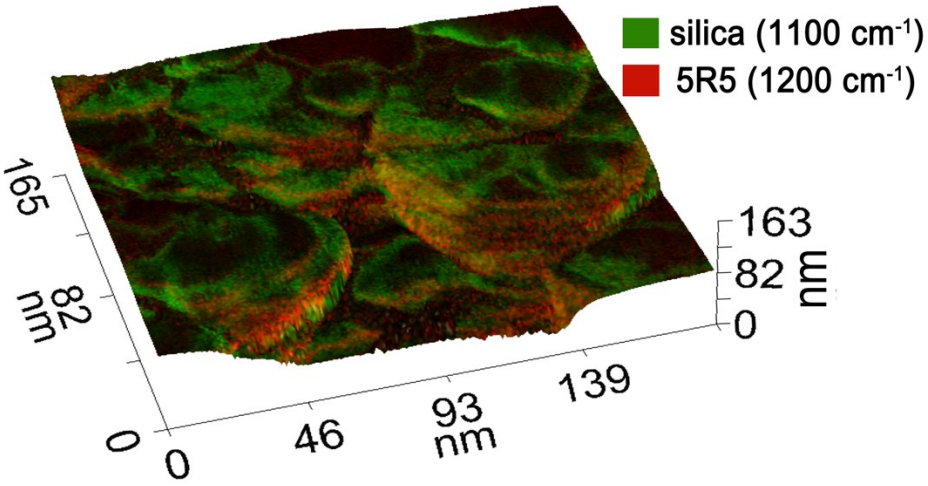

Figure S5. Combined PiFM overlaid on topography. The green features are the silica nanoparticles and the red edges highlight the 5R5 protein.

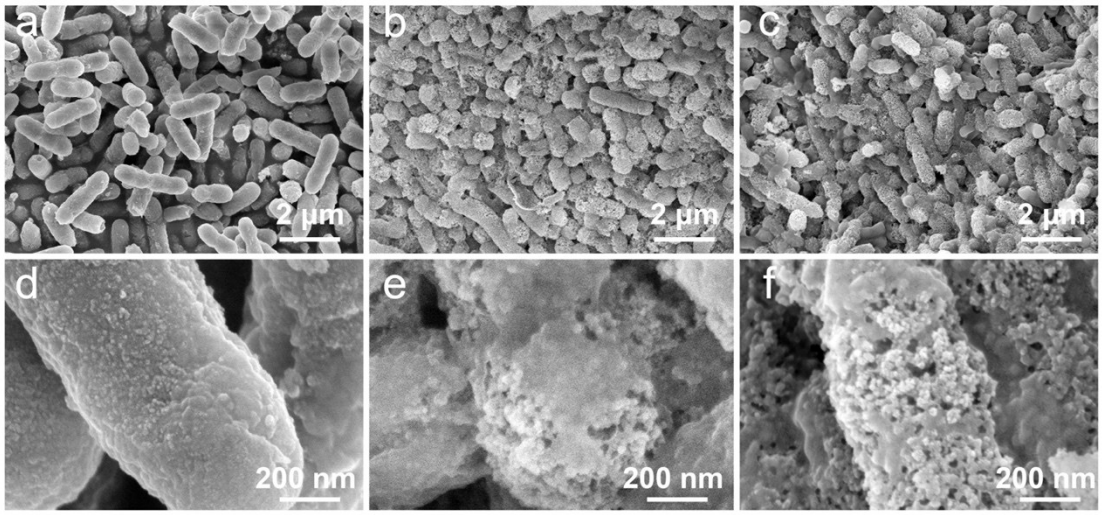

Figure S6. Structure of mineralized bacteria after incubation at 37 °C for 48 hours and 80 °C for different hours. SEM images of (a,d) 24 h, (b,e) 32 h, (c,f) 40 h.

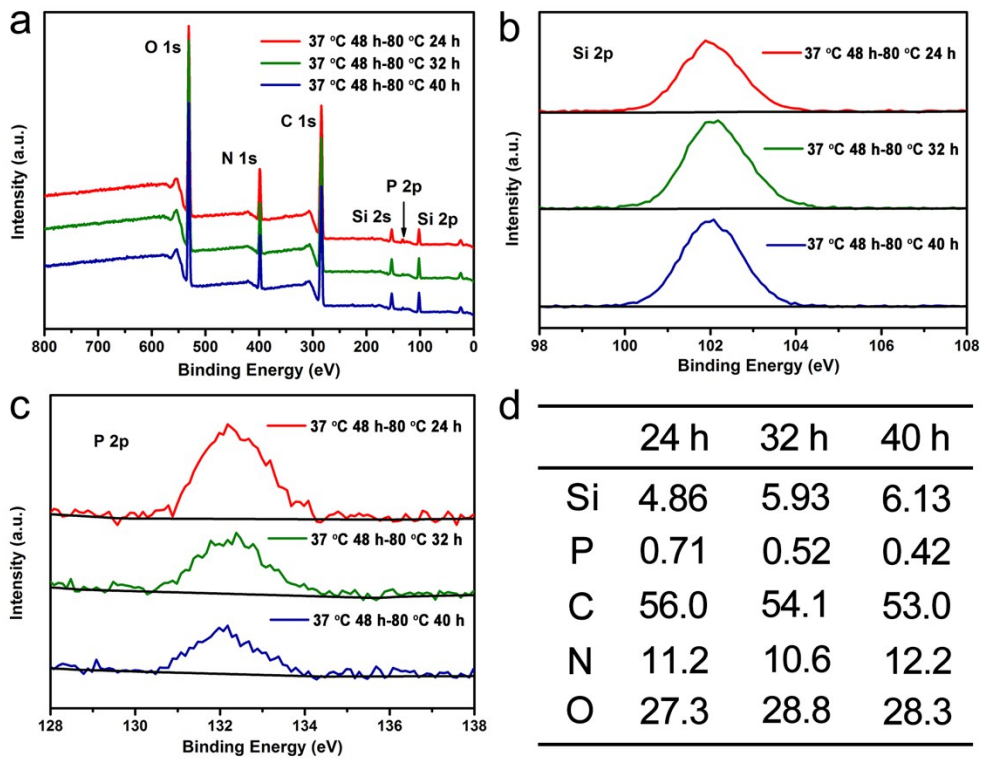

d

	24 h	32 h	40 h
Si	4.86	5.93	6.13
P	0.71	0.52	0.42
C	56.0	54.1	53.0
N	11.2	10.6	12.2
O	27.3	28.8	28.3

Figure S7. XPS spectra of mineralized bacteria after incubation at 37 °C for 48 hours and 80 °C for 24, 32 and 40 hours. (a) The full XPS spectra. High-resolution spectra of (b) Si 2p, and (c) P 2p. (d) The atom ratio of Si, P, C, N and O in the products.

With the increasing reaction time at 80 °C, the Si content is slightly increased; whereas, the amount of P is gradually decreased. The increase of Si content is corresponding to the thermogravimetric analysis (Figure S8). The P element is mainly resourced from the phospholipid in cell membrane. The decrease of P content indicates the break of cell membrane structure. Therefore, the nanoparticles on cell surface are exposed. The increased amount of silica after incubating at 80 °C is attributed to the loss of organics. Combining the thermogravimetric curves and XPS spectra, we conclude that the silicification on cell surface almost completes at 37 °C. The main reasons of continuous reaction at 80 °C are to appropriately reduce the organic content and maintain the rod-shaped structure after calcination efficiently.

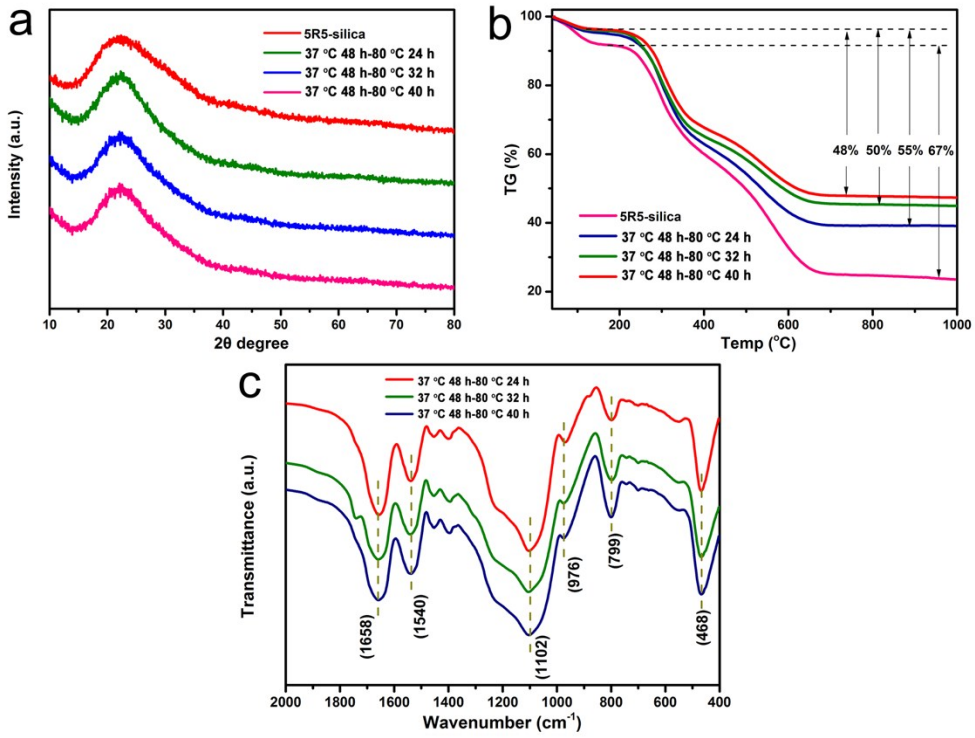

Figure S8. Composition of mineralized bacteria after incubation at 37 °C for 48 hours and 80 °C for 24, 32 and 40 hours. (a) XRD patterns, (b) TG curves and (c) FTIR spectra of mineralized bacteria. The bands at 976 cm^{-1} in FTIR spectra were corresponding to the symmetrical bending vibration of Si-OH. The band at 1658 cm^{-1} was assigned to the characteristic of amide I band of biomolecules in *E. coli*, the sharp band at 1102 cm^{-1} was ascribed to asymmetrical stretching vibration of Si-O-Si.

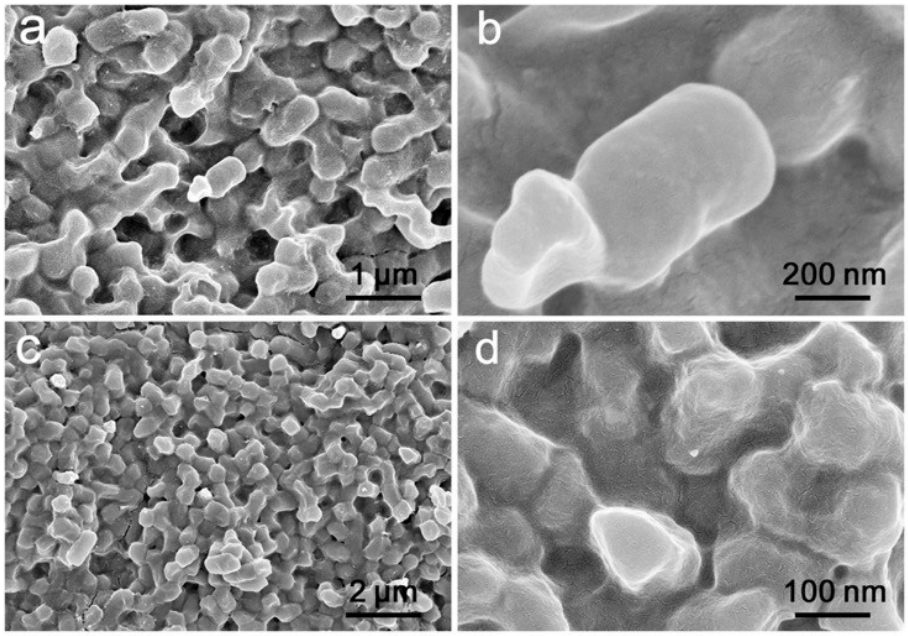

Figure S9. SEM images of wild type bacteria mineralized at 37 °C for 48 hours (a-b), 37 °C for 48 hours and 80 °C for 24 hours (c-d).

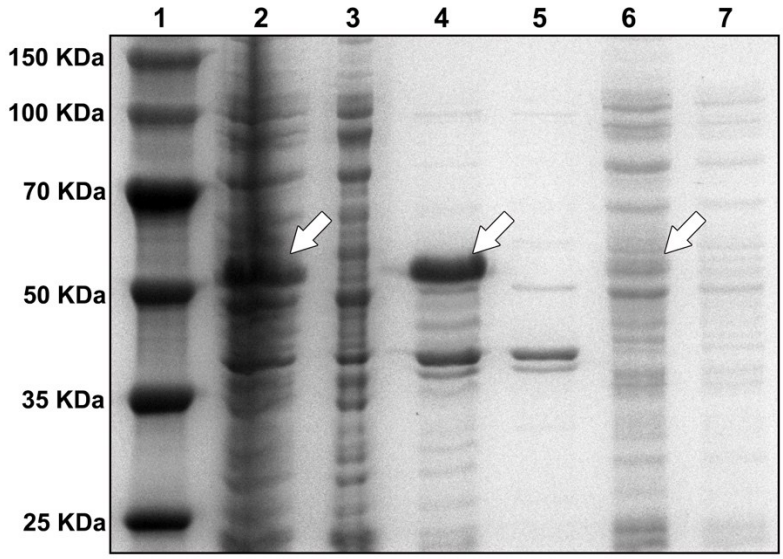

Figure S10. Protein gel electrophoresis of 5R5 modified *E. coli* analyzed with 10% SDS-PAGE. Lane 1, molecular weight marker; lanes 2 and 3, IPTG-induced and un-induced cells, respectively; lanes 4 and 5, membrane protein of IPTG-induced and un-induced cells, respectively; lanes 6 and 7, supernatant of IPTG-induced and un-induced cells, respectively. The target bands were marked by arrows. The target band in lane 6 means the remaining 5R5 protein inside cell.

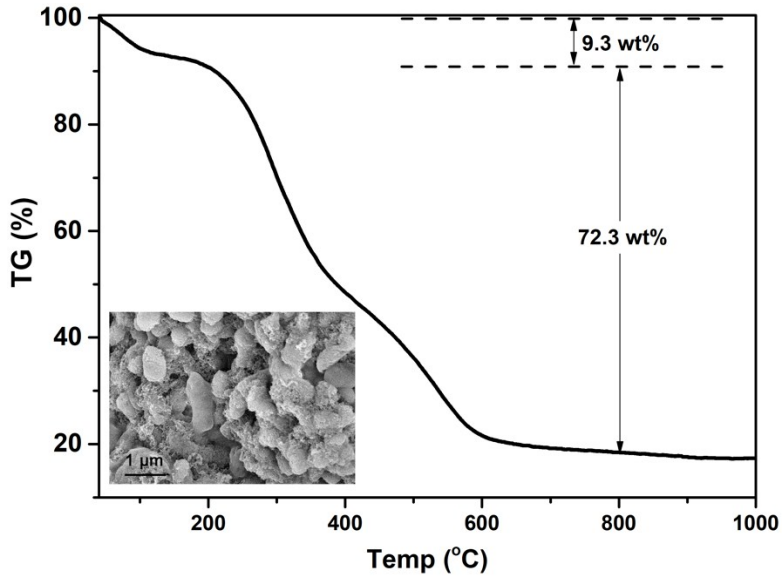

Figure S11. Thermogravimetric curve of silicified *E. coli* with R5 modified at 37 °C for 48 hours (denoted as R5-silica). Inset is the SEM image of R5-silica. Compared with 5R5-silica, the mass loss between 200-800 °C in R5-silica is relatively large. It means the higher ability of mineral-forming activity of 5R5.

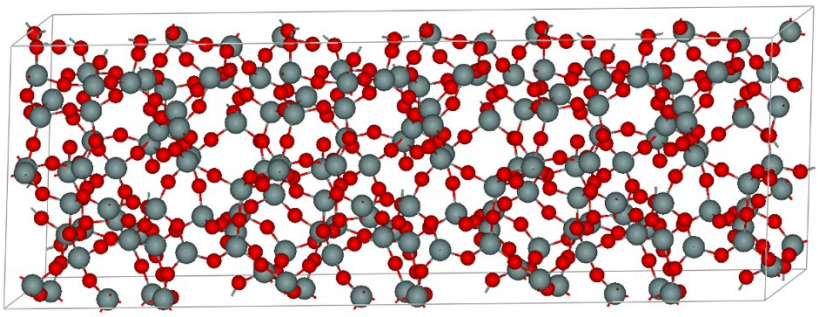

Figure S12. The 311-supercell structure of a-SiO_2 model before functional attachment of CH_2-CH_3 on one side and pacified the dangling bonds of H on the other side.

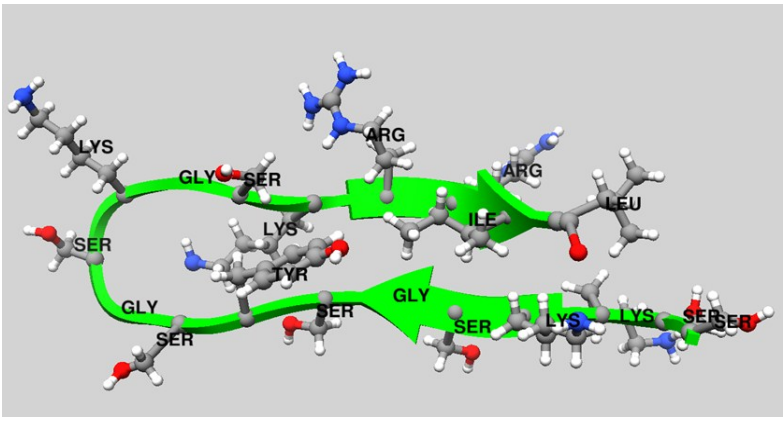

Figure S13. The structure model R5 peptide with amino acid sequence indicated (same as Figure 5c).

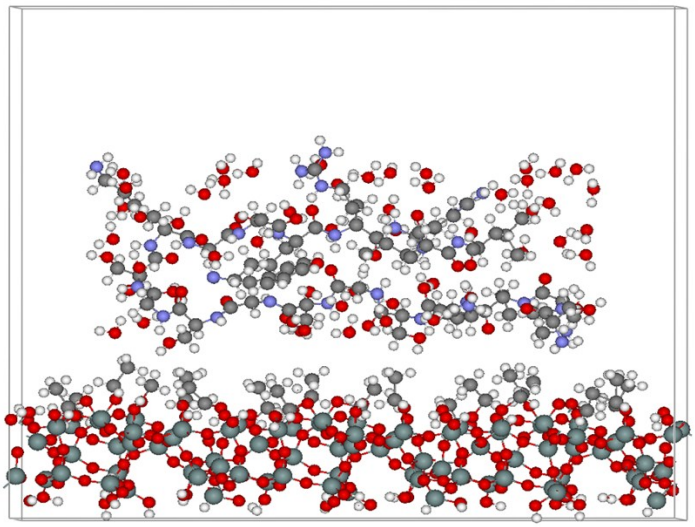

Figure S14. The initial structure model of R5+TEOS including 50 water molecules (same as Figure 3a). Different atomic species have different color: red (O), large gray (Si), small grey (C), blue (N), white (H).

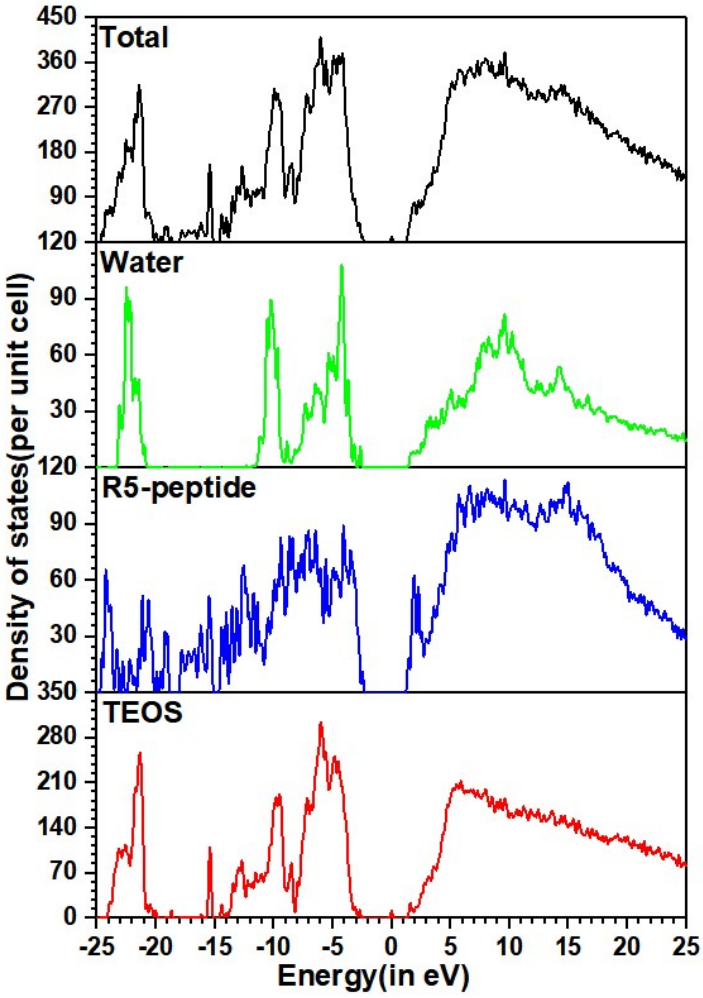

Figure S15. TDOS and PDOS in TEOS+R5 complex.

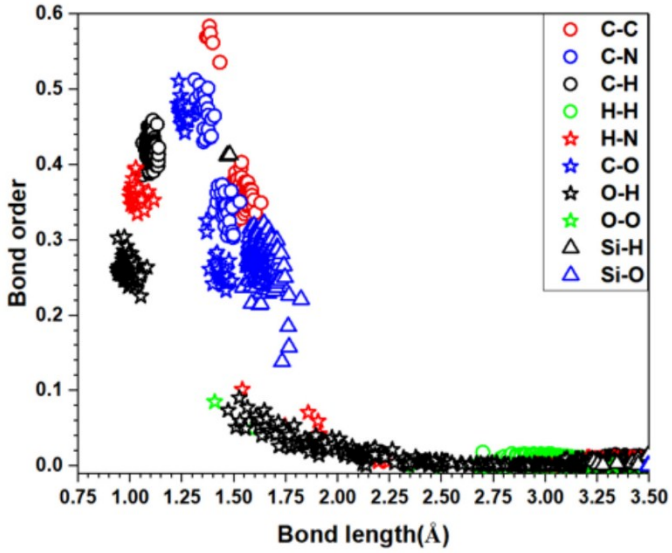

Figure S16. Distribution of BO vs. BL in the final TEOS+R5 model for every pair of atoms in the model. Different types of bonds are indicated. Those with BO less than 0.1 are HBs.

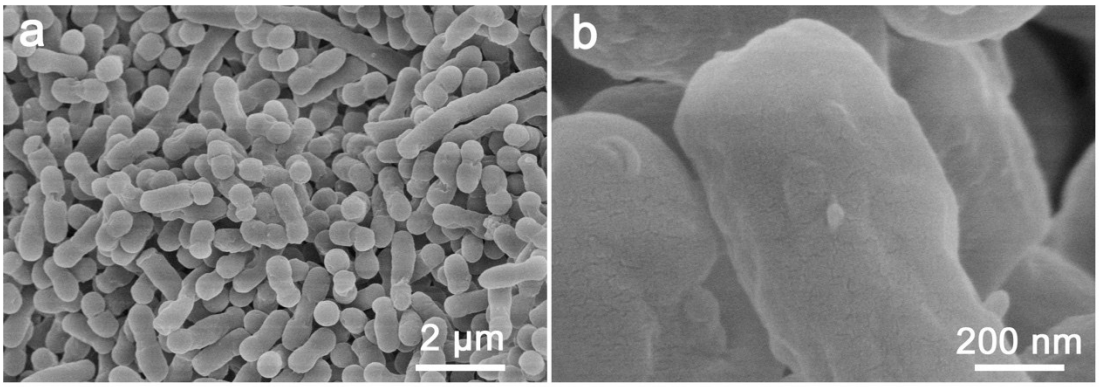

Figure S17. SEM images of silicified cells in anhydrous ethanol. The smooth surface indicates that there is no deposition of silica on the cell surface.

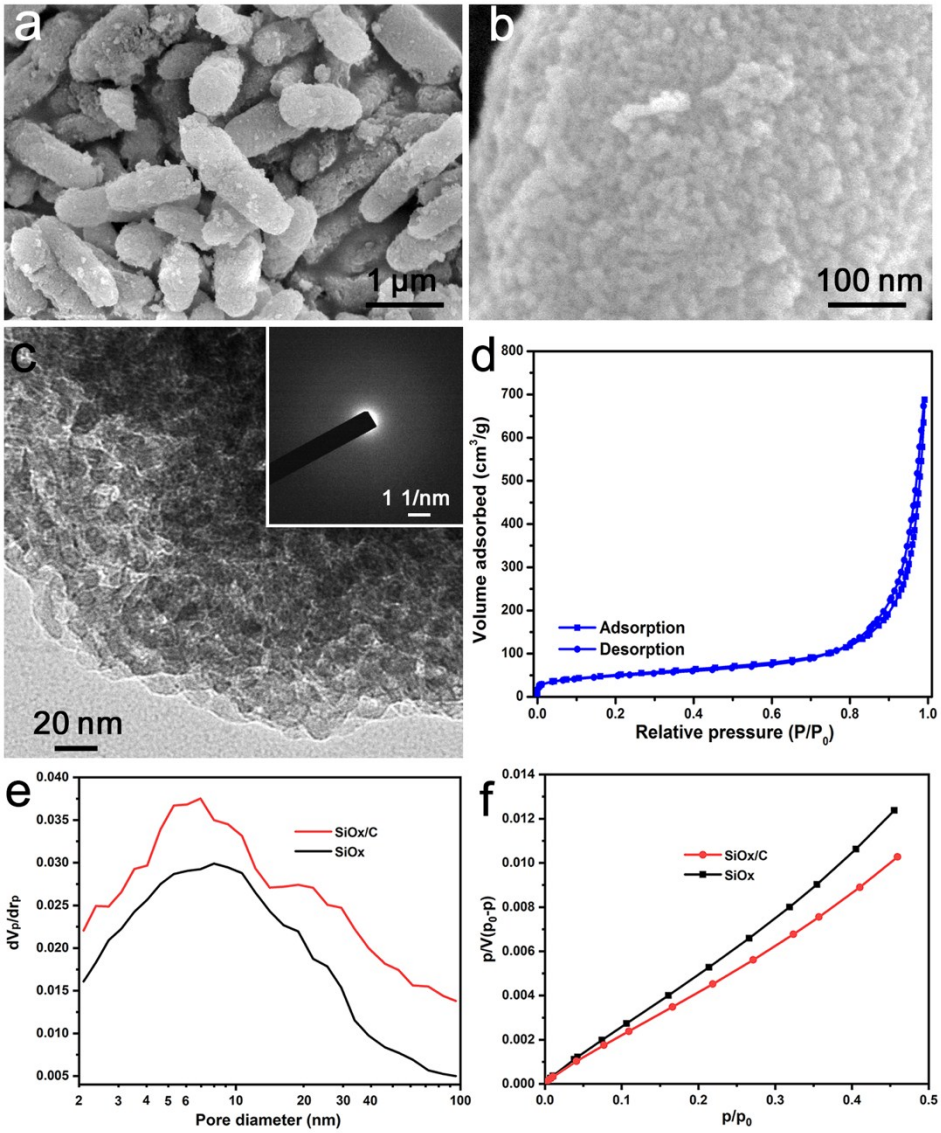

Figure S18. (a-b) SEM images and (c) TEM image of porous SiOx nanorods annealed under air, (c, inset) corresponding SAED pattern. (d) N_2 adsorption-desorption isotherms of SiOx. (e) Pore distribution of SiOx and SiOx/C. (f) linear

approximation of BET analysis of SiOx and SiOx/C.

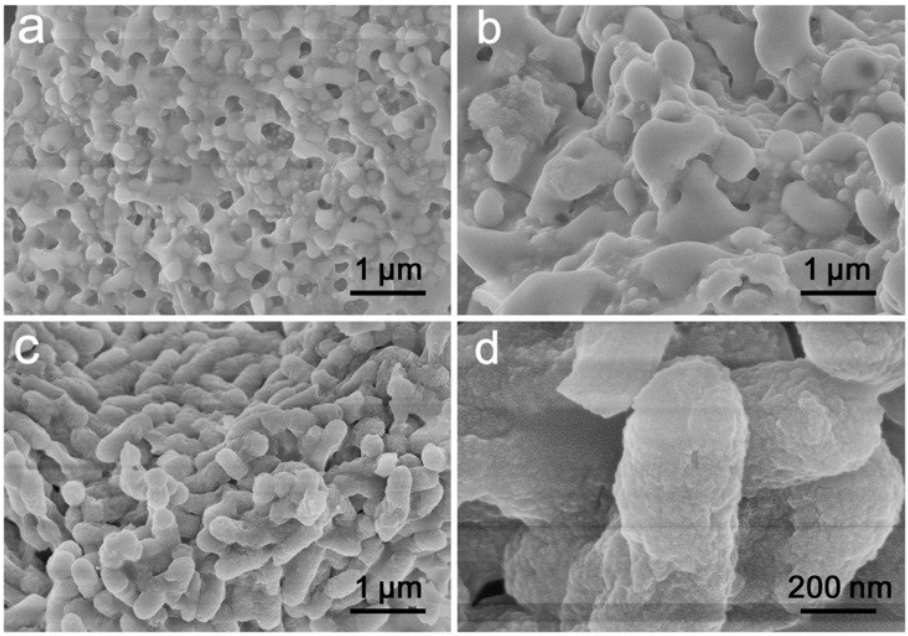

Figure S19. SEM images of mineralized samples after calcination at 800 °C in air. (a) Wild type cells, (b) INP-modified cells, (c-d) INP-5R5 cells were incubated at 37 °C for 48 hours. The organic content in 5R5-silica is relatively high. During calcination, the decomposition of organics will lead a certain degree of collapse, although the rod shape was mainly retained.

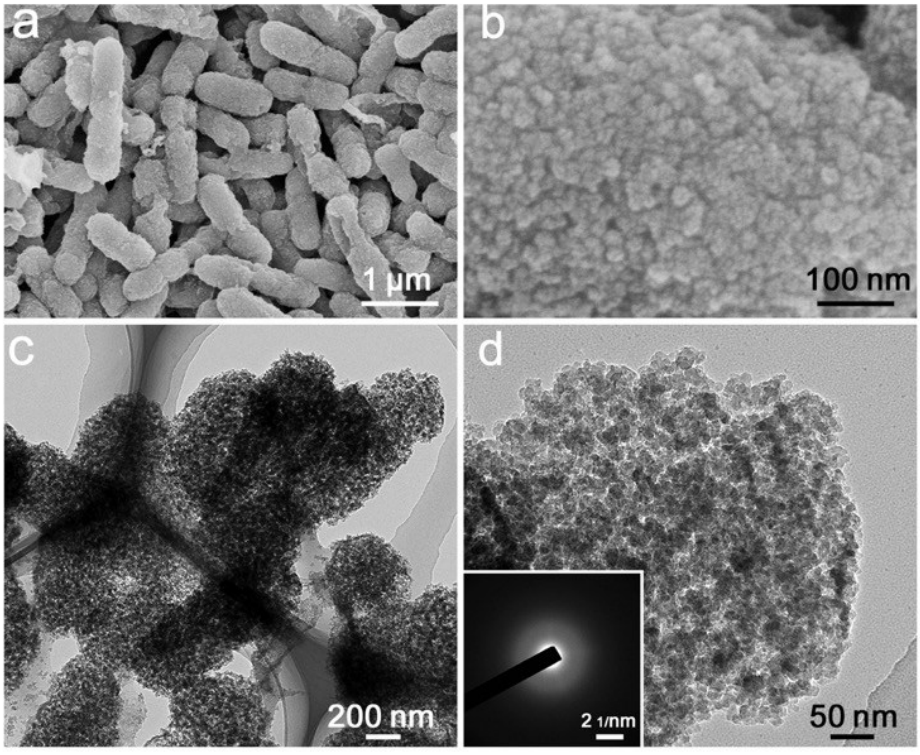

Figure S20. Structure characterization of porous SiOx/C nanorods annealed

under Ar. (a-b) SEM images and (c-d) TEM images, (d, inset) corresponding SAED pattern. Since the organic component in *E. coli* is rich in carbon element, it may serve as carbon source *in situ* during carbonization in inert atmosphere. There were no significant changes of the rod-shaped morphology and nanoparticle size between SiOx and SiOx/C samples.

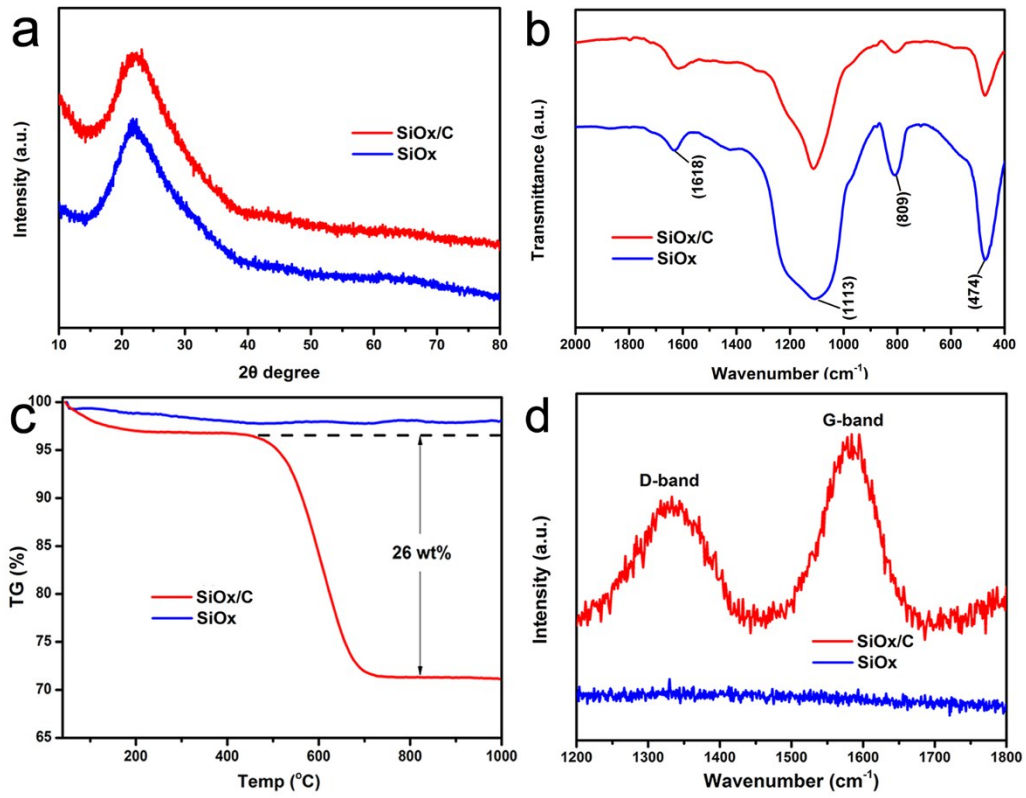

Figure S21. Composition of SiOx and SiOx/C nanorods. (a) XRD patterns. (b) FTIR spectra. The preserved bands at 474 cm^{-1}, 809 cm^{-1} and 1113 cm^{-1} were ascribed to group vibration correlated with silicon and oxygen elements. Owing to the thermal decomposition and carbonization of organic matter, the typical amide bands and bending vibration of Si-OH at 966 cm^{-1} all disappeared. (c) Thermogravimetric curves. The weight loss before 200 °C was attributed to the removal of absorbed water. The weight loss after 200 °C resulted from the combustion of amorphous carbon, and the carbon content was about 26 wt%. (d) Raman spectra. There was no characteristic carbon peak in SiOx.

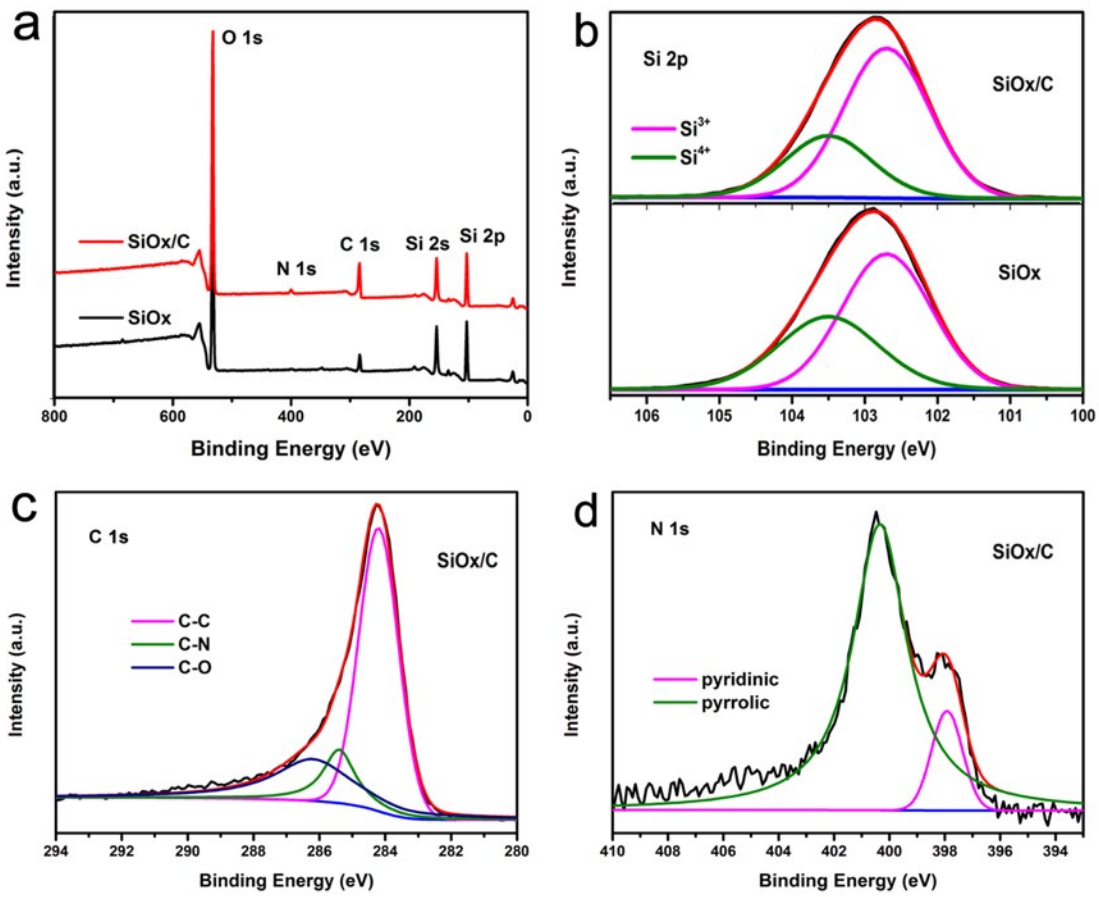

Figure S22. XPS spectra of SiOx and SiOx/C nanorods. (a) The full XPS spectra. High-resolution spectra of (b) Si 2p, (c) C 1s and (d) N 1s.

The high-resolution Si 2p spectra can be deconvoluted into two components: Si^{3+} at 102.7 eV, Si^{4+} at 103.5 eV[2]. The carbon may reduce a small amount of silica at high temperature, so the proportion of Si^{3+} to Si^{4+} in the SiOx/C sample is higher than that in the SiOx sample. The absence of low valence of silicon indicates the high degree of oxidation in samples. The N element is also detected in SiOx/C samples with XPS analysis, but not in SiOx samples. It further confirmed the incorporation of N into carbon coating, which could improve the conductivity of SiOx/C. The N-doped level is about 2.0 at%. The absence of graphitic N in carbon coating meant the nitrogen atoms all occupied the defect sites with dangled electron pairs in carbon[3].

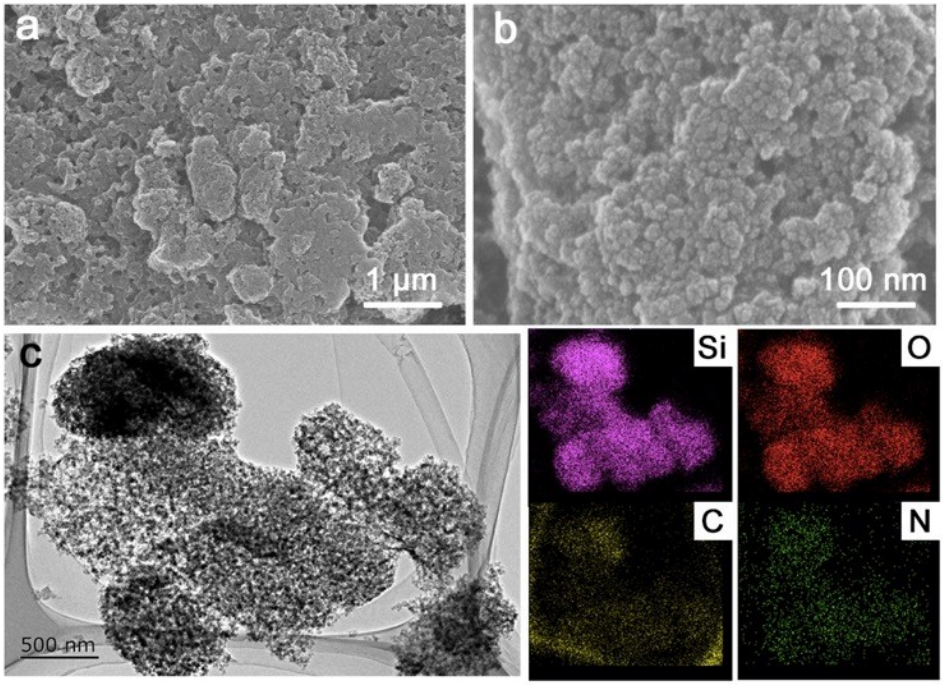

Figure S23. The post-mortem characterization of SiOx/C electrodes after 100 cycles at current rate of 1 A g^{-1}. (a) Low and (b) high magnification SEM images. The nanorod structure is well reserved, and the 10 nm particles on the surface are clearly observed. (c) TEM image and element mapping images of Si, O, C, N. TEM image manifested the porous structure is intact, and the elemental mapping images present a uniform distribution of Si, O, C, and N elements.

The maintenance of structure stability in SiOx/C electrode plays a dominant role for the high reversible capacity and rate capability. In order to explore the advantages of rod-shaped structure, the commercial amorphous silica power (denoted as Com-SiO_2) with a diameter between 8-10 nm was served as a control group (Figure S4e). In the initial charge/discharge cycle, the SiOx/C electrode exhibited a discharge capacity of 2285 mAh g^{-1} with a coulombic efficiency of 41 %, which is higher than that of SiOx (1405 mAh g^{-1}) and Com-SiO_2 (1051 mAh g^{-1}). The low coulombic efficiency could be ascribed to the formation of SEI layer and the side reaction between lithium and active materials[4]. Under the same conditions, the rate capabilities of SiOx anode (572.5, 538, 446.5, 381, 311.5 and 226.3 mA h g^{-1}) and commercial amorphous silica power (denoted as Com-SiO_2) anode (346.7, 268.7, 190.6, 146.8, 118.7, and 95.9 mA h g^{-1}) were much lower than those of SiOx/C anode.

In comparing with Com-SiO_2, the nanostructured SiOx is composed of nanoparticles with the same size. The higher lithium storage performance of SiOx is attributed the nanorod with mesoporous structure. During the charge/discharge process, the mesoporous structure is beneficial to accommodate the volume variation and prohibit the structure collapse. While, the aggregation of nanoparticles in Com-SiO_2 during cycling may suppress the alloying/dealloying between Li^+ ions and active materials, which declining the capability of lithium storage. In comparing with SiOx, the presence of N-doped

carbon coating on nanoparticles increases the specific surface area, which providing more active sites for the reaction between liquid electrolyte and SiOx/C. In addition, the promotion of electronic conductivity can accelerate the transportation of electrons and Li^+ ions. Therefore, the SiOx/C electrode exhibits superior specific capacity and rate capability than SiOx and Com-SiO_2 electrodes.

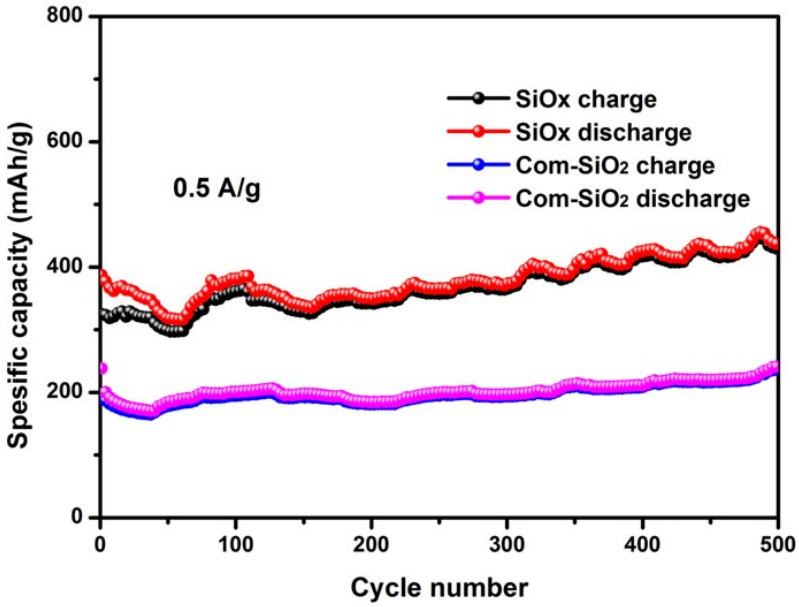

Figure S24. Cycling performance of SiOx and Com-SiO_2 electrodes at a current rate of 0.5 A g^{-1}.

The repeating charging-discharging process may promote the penetration of electrolyte into the central region of nanorods. The enlarged contact area of active materials will be utilized to react with electrolyte, which leads to an increased capacity. The same phenomenon was recurred in SiOx electrode, which delivers a discharge capacity of 437.4 mA h g^{-1} after 500 cycles. Whereas, the specific capacity of Com-SiO_2 electrode was almost constant, its discharge capacity was determined to 240.6 mA h g^{-1} after 500 cycles.

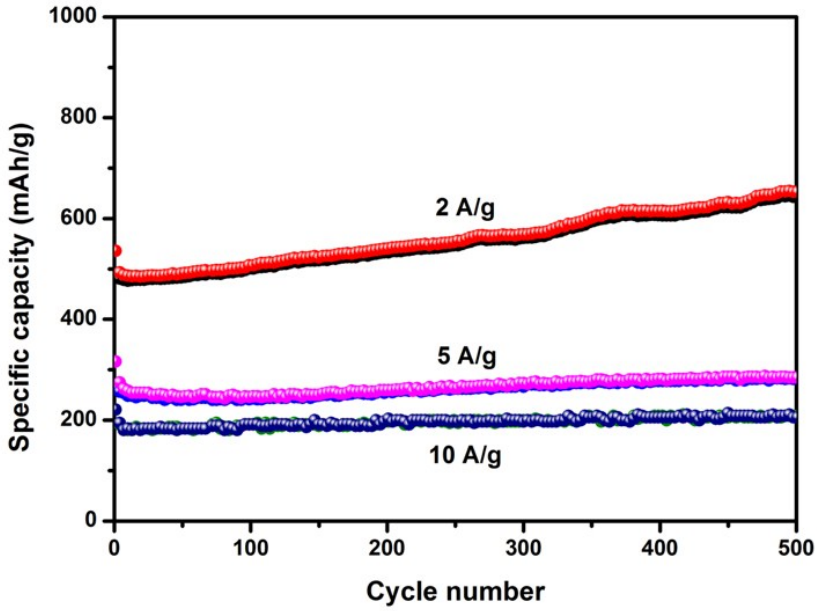

Figure S25. Cycling performance of SiOx/C electrode at a current rate of 2, 5 and 10 A g^{-1}.

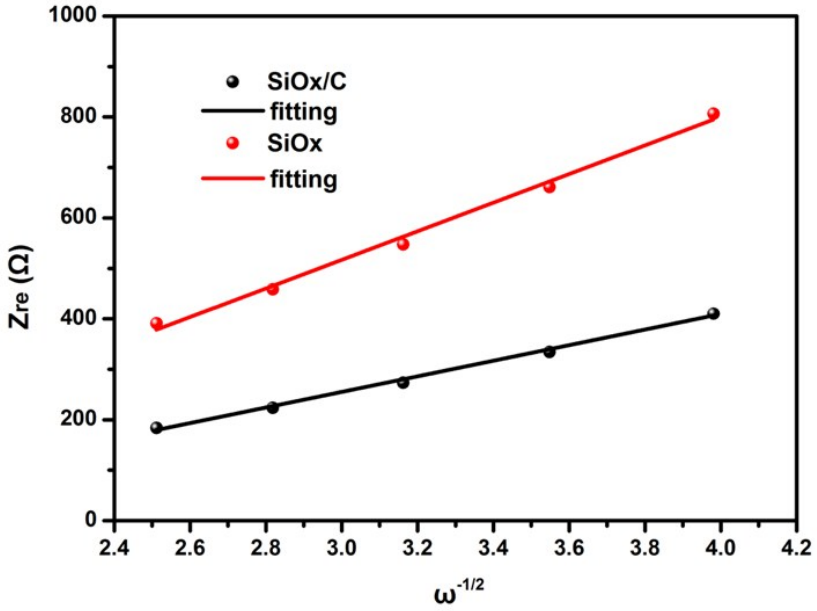

Figure S26. The relationship and fitting results between Zre plotted against $\omega^{-0.5}$ in SiOx/C and SiOx.

The Nyquist plots are comprised by semicircular region and linear Warburg region, located at high-to-medium and low frequency, respectively. The Rct is related to the charge transfer resistance, and the fitting results suggest that the Rct in SiOx/C electrode (26.8 Ω) is smaller than that of SiOx electrode (82.0 Ω). The result indicates that the carbon layer improves the conductivity in hybrid

system.

The Warburg region is associated with the Li^+ apparent diffusion coefficient (D_{Li+}), which can be calculated according to the equation $D_{Li+} = R^2T^2/2A^2n^4F^4C^2\sigma^2$. In the content's equation, where R is the gas constant, T is the absolute temperature, A is the surface area of the electrode, n is the number of electrons per molecule during oxidization, F is the Faraday constant, C is the Li^+ concentration, and σ is the Warburg factor associated with Z′ ($Z' \propto \sigma\omega^{-1/2}$).

Table S1. Comparison of electrochemical performance of various SiOx based anodes.

Electrode materials	Specific capacity (mA h g^{-1})	Discharge rate	Voltage range	References
Bimodal porous carbon-silica	611 (after 200 cycles) 313 (after 1500 cycles)	0.2 A g^{-1} 3 A g^{-1}	0.01-3 V	5
Graphite-like SiOx/C	645 (after 500 cycles)	0.325 A g^{-1}	0.005-2 V	6
Nanosilica/carbon composite	620 (after 300 cycles)	0.1 A g^{-1}	0-3 V	7
Carbon-coated SiOx nanowires	1060 (after 100 cycles) 623 (after 150 cycles)	0.1 A g^{-1} 0.5 A g^{-1}	0.01-3 V	8
Ni-functionalized SiO_2 hollow spheres	676 (after 50 cycles) 337 (after 1000 cycles)	0.1 A g^{-1} 10 A g^{-1}	0.01-3 V	4
Graphene encapsulated SiOx	780 (after 1000 cycles)	1 A g^{-1}	0.01-3 V	9
SiOx Nanodandelion	960 (after 800 cycles)	0.2 A g^{-1}	0-1 V	10
Ultra-thin SiOx	760 (after 400 cycles)	0.5 A g^{-1}	0.01-2 V	11
SiOx/carbon composites	541 (after 600 cycles)	0.2 A g^{-1}	0.005-2 V	12
Ultrafine SiOx/carbon framework	540 (after 200 cycles)	0.5 A g^{-1}	0.01-1.5 V	13
SiOx/C nanorods	975.8 (after 500 cycles) 791.7 (after 100 cycles) 205.5 (after 500 cycles)	0.5 A g^{-1} 1 A g^{-1} 10 A g^{-1}	0.01-3 V	Our work

Supplementary References

1. S. Y. Lee, J. H. Choi and Z. H. Xu, Trends Biotechnol, 2003, 21, 45-52.
2. C. Yang, Y. Zhang, J. Zhou, C. Lin, F. Lv, K. Wang, J. Feng, Z. Xu, J. Li and S. Guo, J Mater Chem A, 2018, 6, 8039-8046.
3. P. Błoński, J. Tuček, Z. Sofer, V. Mazánek, M. Petr, M. Pumera, M. Otyepka and R. Zbořil, J Am Chem Soc, 2017, 139, 3171-3180.
4. C. Tang, Y. Liu, C. Xu, J. Zhu, X. Wei, L. Zhou, L. He, W. Yang and L. Mai, Adv Funct Mater, 2018, 28, 1704561.
5. Z. Qiang, X. Liu, F. Zou, K. A. Cavicchi, Y. Zhu and B. D. Vogt, J Phys Chem C, 2017, 121, 16702-16709.
6. Q. Xu, J.-K. Sun, Y.-X. Yin and Y.-G. Guo, Adv Funct Mater, 2018, 28, 1705235.

7. M. Li, Y. Yu, J. Li, B. Chen, X. Wu, Y. Tian and P. Chen, J Mater Chem A, 2015, 3, 1476-1482.
8. Z. Li, Q. He, L. He, P. Hu, W. Li, H. Yan, X. Peng, C. Huang and L. Mai, J Mater Chem A, 2017, 5, 4183-4189.
9. Q. Xu, J.-K. Sun, Z.-L. Yu, Y.-X. Yin, S. Xin, S.-H. Yu and Y.-G. Guo, Adv Mater, 2018, 30, 1707430.
10. X. Luo, H. Zhang, W. Pan, J. Gong, B. Khalid, M. Zhong and H. Wu, Small, 2015, 11, 6009-6012.
11. L. Sun, T. Su, L. Xu, M. Liu and H.-B. Du, Chem Commun, 2016, 52, 4341-4344.
12. Q. Xu, J.-K. Sun, G. Li, J.-Y. Li, Y.-X. Yin and Y.-G. Guo, Chem Commun, 2017, 53, 12080-12083.
13. Z. Sun, X. Wang, T. Cai, Z. Meng and W.-Q. Han, RSC Adv, 2016, 6, 40799-40805.